Chemical Science

ROYAL SOCIETY OF CHEMISTRY

EDGE ARTICLE

View Article Online
View Journal | View Issue

Cite this: *Chem. Sci.*, 2022, **13**, 7057

All publication charges for this article have been paid for by the Royal Society of Chemistry

Vibronic effects accelerate the intersystem crossing processes of the through-space charge transfer states in the triptycene bridged acridine–triazine donor–acceptor molecule TpAT-tFFO†

Jeremy M. Kaminski, [a] Angela Rodríguez-Serrano, [a] Fabian Dinkelbach,[a] Hector Miranda-Salinas, [b] Andrew P. Monkman [b] and Christel M. Marian *[a]

Quantum chemical studies employing combined density functional and multireference configuration interaction methods suggest five excited electronic states to be involved in the prompt and delayed fluorescence emission of **TpAT-tFFO**. Three of them, a pair of singlet and triplet charge transfer (CT) states (S_1 and T_1) and a locally excited (LE) triplet state (T_3), can be associated with the (Me → N) conformer, the other two CT-type states (S_2 and T_2) form the lowest excited singlet and triplet states of the (Me → Ph) conformer. The two conformers, which differ in essence by the shearing angle of the face-to-face aligned donor and acceptor moieties, are easily interconverted in the electronic ground state whereas the reorganization energy is substantial in the excited singlet state, thus explaining the two experimentally observed time constants of prompt fluorescence emission. Forward and reverse intersystem crossing between the singlet and triplet CT states is mediated by vibronic spin–orbit interactions involving the LE T_3 state. Low-frequency vibrational modes altering the distance and alignment of the donor and acceptor π-systems tune the S_1 and T_3 states (likewise S_2 and T_3) into and out of resonance. The enhancement of intersystem crossing due to the interplay of vibronic and spin–orbit coupling is considered a general feature of organic through-space charge-transfer thermally activated delayed fluorescence emitters.

Received 20th December 2021
Accepted 16th February 2022

DOI: 10.1039/d1sc07101g

rsc.li/chemical-science

1 Introduction

Recently, Kaji and co-workers[1] presented combined experimental and theoretical studies of **TpAT-tFFO**, a thermally activated delayed fluorescence (TADF) emitter constituted by 9,9-dimethyl-9,10-dihydroacridine as a donor (**A**), 2,4-diphenyl-1,3,5-triazine as an acceptor (**T**) and triptycene (**Tp**) as a bridge connecting the subunits **A** and **T** in a tilted face-to-face (**tFF**) configuration with optimal (**O**) distance (Fig. 1).

A key feature of a TADF emitter is an efficient reverse intersystem crossing (rISC) from the triplet manifold to the first excited singlet state by which triplet as well as singlet excitons can be harvested in an organic light-emitting diode (OLED). In principle, therefore internal quantum efficiencies of up to 100% can be reached in a TADF OLED. Because of the through-space configuration of the donor and acceptor moieties in **TpAT-tFFO** ($d_{DA} = 4.72$ Å), the spatial overlap between HOMO and LUMO is very small which in turn leads to a minuscule energy separation between the lowest excited singlet and triplet states. While a small singlet–triplet energy gap ($\Delta E_{ST} < 0.1$ eV) is favorable for thermally activated processes such as rISC, the negligible spatial overlap of the hole and particle densities results in a moderate $S_1 \rightarrow S_0$ transition dipole moment in accordance with the comparably low fluorescence rate constant of $k_F = 1.1 \times 10^6$ s^{-1} deduced from experiment.[1] With ISC and rISC rate constants of $k_{ISC} = 5.2 \times 10^7$ s^{-1} and $k_{rISC} = 1.2 \times 10^7$ s^{-1}, respectively, at room temperature (RT) in doped film, the ISC

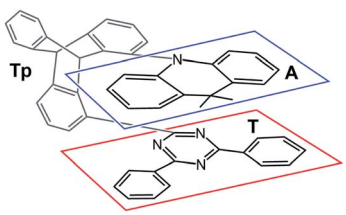

Fig. 1 Chemical structure **TpAT-tFFO** with its donor (**A**, blue box), acceptor (**T**, red box), and linker (**Tp**, unframed) subunits.

[a]*Institute of Theoretical and Computational Chemistry, Heinrich-Heine-University Düsseldorf, D-40204 Düsseldorf, Germany. E-mail: christel.marian@hhu.de*

[b]*Dept of Physics, OEM Research Group, Durham University, Durham, DH1 3LE, UK. E-mail: a.p.monkman@durham.ac.uk*

† Electronic supplementary information (ESI) available: Details of the electronic structure data, TDDFT energies, scans along normal modes and linearly interpolated paths, spin–orbit coupling matrix elements and their derivatives with respect to normal modes. See **https://doi.org/10.1039/d1sc07101g**

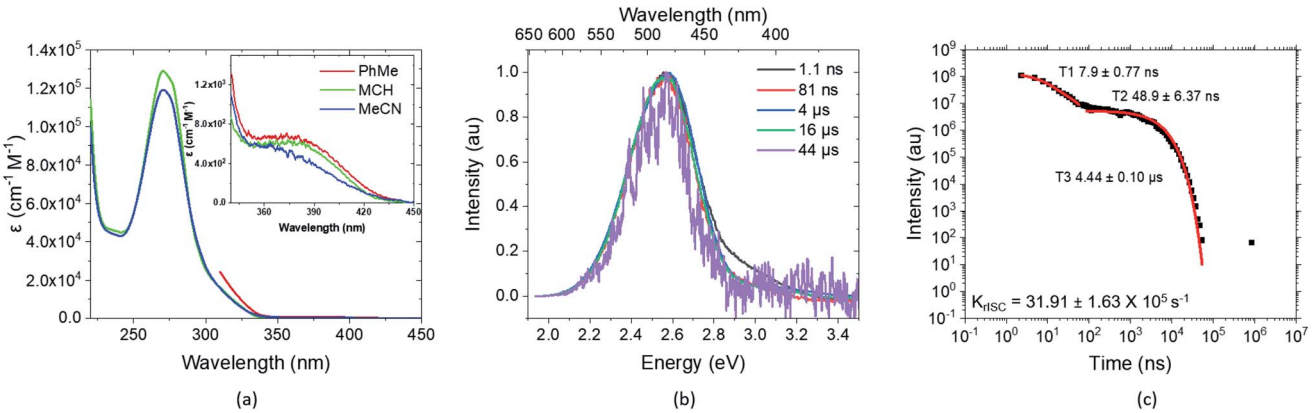

Fig. 2 Experimental key results on the photophysics of TpAT-tFFO, presented in detail in ref. 2. (a) Extinction coefficients in different solvents and close-up of the direct CT absorption band in the inset, (b) time-resolved spectral frames of the PhMe degassed solution at different times and (c) decay, lifetimes and k_{rISC} of the same PhMe solution (all solution concentrations are 20 μM L^{-1}).

and rISC processes are an order of magnitude faster than prompt fluorescence in this molecule, *i.e.*, the excited singlet and triplet populations can largely equilibrate before emitting delayed fluorescence with a radiative lifetime of 4.1 μs.[1]

Newer time-resolved measurements in various solvents and host matrices by Monkman and coworkers, described in detail in a forthcoming publication,[2] suggest the excitation decay kinetics to be even more involved. Two components for the decay of prompt fluorescence with different time constants but essentially identical emission wavelengths are observed followed by delayed fluorescence in degassed solution at RT (Fig. 2). In mCBP host, in addition strong long-lived phosphorescence emission is seen at 20 K. While the absolute S_1 and T_1 energies change from host to host, their energy separation ΔE_{ST} stays surprisingly constant at about 0.016 ± 0.002 eV.[2] These intriguing experimental observations call for a detailed quantum chemical study of the **TpAT-tFFO** donor–acceptor complex that can shed light on its excited-state decay processes.

Because ISC and rISC between singlet and triplet charge-transfer (CT) states of equal electronic structure are orbitally forbidden, spin–vibronic coupling with a nearby locally excited (LE) triplet state has been argued to be essential for enhancing the radiationless ^{1}CT ↔ ^{3}CT transitions in both, through-bond and through-space donor–acceptor complexes.[1,3–12] Quantum chemical calculations on **TpAT-tFFO** in the framework of time-dependent density functional theory (TDDFT)[1] suggest the presence of a ^{3}LE state on the **T** acceptor in close energetic proximity of the lowest-lying ^{1}CT and ^{3}CT states. The results of this study further indicate that a tilted face-to-face (tFF) alignment of **A** and **T** gives rise to stronger spin–orbit coupling (SOC) between ^{1}CT and ^{3}LE (0.61 cm^{-1}) than the parallel face-to-face (pFF) alignment (0.05 cm^{-1}) of the donor and acceptor moieties while the SOC between ^{1}CT and ^{3}CT vanishes (0.00 cm^{-1}) in both conformations. Therefore, spin–vibronic effects are expected to play an essential role in the ISC and rISC transitions of this TADF emitter. This three-state model can, however, not explain the bi-exponential decay of the prompt fluorescence observed in the newer time-resolved experiments by the Monkman group.[2] To elucidate the mechanisms underlying the considerably fast ISC and rISC of **TpAT-tFFO** found in experiment, we have characterized the electronic structures of its low-lying singlet and triplet states in the framework of density functional theory (DFT) and multi-reference configuration interaction (MRCI) methods and explored their interactions by means of associated spin–orbit coupling and property programs. The chosen computational protocol has proven to yield energies and rate constants that are sufficiently accurate to provide valuable insights into the kinetics of competitive radiative and nonradiative decay processes.[13–17]

2 Computational methods

Electronic ground-state geometries of the **TpAT-tFFO** emitter were optimized using the Turbomole program package[18] and DFT at the PBE0-D3(BJ)/def2-SV(P) level of theory[19,20] including Grimme's dispersion correction (D3) together with Becke and Johnson (BJ) damping.[21,22] Time-dependent DFT (TDDFT) was used for the optimization of the excited singlet states[23–26] while the Tamm–Dancoff approximation (TDA) was utilized for the optimization of the excited triplet states.[27] Analytic harmonic vibrational frequencies were computed by means of Gaussian16.[28]

Vertical and adiabatic excitation energies and optical electronic properties were calculated using the DFT/MRCI method.[29–31] Up to 25 roots at the respective ground-state geometries and 10 roots at the excited-state geometries were determined for each singlet and triplet manifold in DFT/MRCI employing closed-shell BH-LYP[32,33] orbitals as the one-particle basis. The parametrization of the Hamiltonian reported in Lyskov *et al.*[34] for the tight configuration selection threshold of $0.8E_h$ was employed (DFT/MRCI-R2016), which is specially designed for large multichromophoric systems. Fragment-based analyses of the singlet and triplet DFT/MRCI wavefunctions were performed by an extended version of the TheoDORE tool box.[17,35] Mutual spin–orbit coupling matrix elements (SOCMEs) between target singlet and triplet states were calculated with the spin–orbit coupling kit (SPOCK) developed in our group.[36–38] Here, the SOC is described by using the Breit–Pauli

Hamiltonian and the atomic spin–orbit mean-field approximation.[39,40] Rate constants for ISC and rISC between excited singlet and triplet states were determined in the framework of Fermi's golden rule approximation and a time-dependent Fourier transform approach as implemented in the VIBES program.[41,42] Temperature effects were accounted to the rate constants by assuming a Boltzmann distribution in the initial electronic state. In the Franck–Condon (FC) approximation, the rate constant for the $S_a \rightsquigarrow T_b$ ISC at a given temperature T is computed as the sum of squared electronic SOCMEs between the initial singlet state S_a at its minimum geometry Q_0 and the three triplet sublevels $T_b{}^{\alpha}$, multiplied by the Boltzmann and FC weighted density of vibrational states according to[41]

$$k_{\mathrm{ISC_{ab}}}^{\mathrm{FC}}(T) = \frac{2\pi}{\hbar Z}\sum_{\alpha}\left|\left\langle \Psi_{\mathrm{T}_b{}^{\alpha}}\middle|\hat{\mathcal{H}}_{\mathrm{SO}}\middle|\Psi_{\mathrm{S}_a}\right\rangle\right|^2_{Q_0} \times \sum_k \mathrm{e}^{\frac{-(E_{ak}-E_{a0})}{k_{\mathrm{B}}T}}\sum_j \left|\left\langle v_{bj}\middle|v_{ak}\right\rangle\right|^2 \delta\left(E_{ak}-E_{bj}\right). \quad (1)$$

here k_{B} is the Boltzmann constant and $Z = \sum_k \mathrm{e}^{\frac{-(E_{ak}-E_{a0})}{k_{\mathrm{B}}T}}$ the partition function of the initial state. In the Herzberg–Teller (HT) approximation, the SOC is expanded as a function of the normal coordinates Q of the initial state about Q_0 and the expansion is terminated after the linear term.[8,43,44]

$$k_{\mathrm{ISC_{ab}}}^{\mathrm{FC+HT}}(T) = \frac{2\pi}{\hbar Z}\left|\sum_{\alpha}\sum_k e^{\frac{-(E_{ak}-E_{a0})}{k_{\mathrm{B}}T}}\sum_j \left\langle v_{bj}\middle|\left\langle \Psi_{\mathrm{T}_b{}^{\alpha}}\middle|\hat{\mathcal{H}}_{\mathrm{SO}}\middle|\Psi_{\mathrm{S}_a}\right\rangle\right.\right|_{Q_0} + \sum_A \left.\frac{\partial\left\langle \Psi_{\mathrm{T}_b{}^{\alpha}}\middle|\hat{\mathcal{H}}_{\mathrm{SO}}\middle|\Psi_{\mathrm{S}_a}\right\rangle}{\partial Q_{\mathrm{A}}}\right|_{Q_0} Q_{\mathrm{A}}\left|v_{ak}\right\rangle\Big|^2 \delta\left(E_{ak}-E_{bj}\right) \quad (2)$$

Squaring this expression yields a pure FC term, a mixed FC/HT term and a HT/HT term. Similar formulas result for the reverse $S_a \leftarrow T_b$ process. The SOCME gradients in eqn (2) were determined by averaged two-point finite difference techniques. To this end, the nuclear framework was deflected from the respective minimum geometry in positive and negative directions of the dimensionless vibrational normal modes utilizing a step size of 0.1 units. Phase corrections were applied as described in earlier work.[17]

To check whether vibronic effects accelerate fluorescence as well, electric dipole transition moments and their numerical derivatives were employed to compute fluorescence in FC and HT approximation. Because the HT spectra are not properly normalized in the VIBES program, we made use of the closure relation for FC factors to normalize the HT spectrum and to determine fluorescence rate constants according to

$$k_{\mathrm{F}}^{\mathrm{HT}} = \int I^{\mathrm{HT}}(\omega)\mathrm{d}\omega = \frac{4}{3\hbar {c_0}^3}\frac{\int \omega^3 S^{\mathrm{HT}}(\omega)\mathrm{d}\omega}{\int S^{\mathrm{FC}}(\omega)\mathrm{d}\omega} \quad (3)$$

where $I^{\mathrm{HT}}(\omega)$ is the frequency dependent intensity of the computed HT spectrum, $\hbar$ is Planck's constant divided by 2π, c_0 is the vacuum speed of light and $S^{\mathrm{HT}}(\omega)$ and $S^{\mathrm{FC}}(\omega)$ are the HT and FC spectral densities, respectively. Phosphorescence rate constants were determined in FC approximation using multi-reference spin–orbit configuration interaction (MRSOCI)[38] wavefunctions.

3 Computational results

3.1 Ground state

3.1.1 Conformer geometries. The optimization of the electronic ground state led to two different conformations (Fig. 3) which are almost energetically degenerate at DFT/MRCI-R2016 level of theory (ΔE = 0.02 eV). A very shallow barrier separates the S_0 potential energy well of the (Me → N) conformer (Fig. 3 left) from the one of the slightly more stable (Me → Ph) conformer (Fig. 3 right). Vibrational mode 1 (Fig. S1†), which transforms the two ground state conformers into one another, exhibits a harmonic frequency of merely 8 cm^{-1}. Unless hindered by a rigid environment, the two conformers should be easily interconvertable in the electronic ground state at RT.

3.1.2 Absorption spectra. The absorption spectrum measured in apolar solvents and our computed vertical absorption spectra (Fig. 4) match very well, thus validating the computation protocol. The measurements cover a spectral range between *ca.* 250 and 450 nm. Two transitions, namely S_2

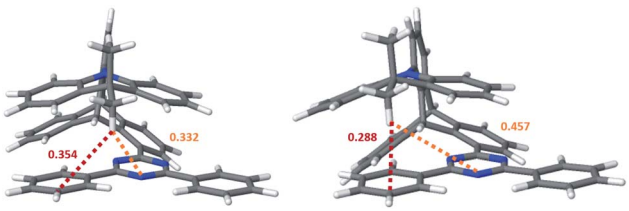

Fig. 3 Nuclear arrangements at the two ground state minima of **TpAT-tFFO** optimized at PBE0-D3(BJ)/def2-SV(P) level of theory (left: S_0(Me → N); right: S_0(Me → Ph)). Distances between the proximal methyl hydrogen atom of the **A** donor and the triazine (orange) or phenyl (red) rings of the **T** acceptor are given in nm.

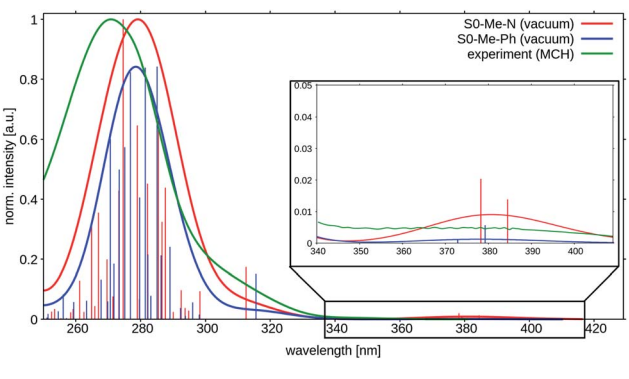

Fig. 4 Vertical absorption spectra at the two ground state minima of **TpAT-tFFO** at the DFT/MRCI-R2016 level of theory *in vacuo* (red: S_0(Me → N), blue: S_0(Me → Ph)). The experimental UV-vis absorption spectrum of **TpAT-tFFO** (green) was recorded in MCH solution at RT. For details. See ref. 2.

← S_0 and S_1 ← S_0, contribute to the weak band in the long wavelength regime. Both result from **A**-to-**T** CT transitions, with the electron density being transferred to the one or the other side of the **T** acceptor (*ca.* Fig. S4 and S7†). The calculations find three triplet states in this wavelength regime, too. T_1 and T_2 are CT states which exhibit very similar electron density distributions as their singlet counterparts whereas T_3 has predominantly LE(**T**) character. The low energy regime is the only part of the spectrum where the two conformers show marked variations. In particular, the oscillator strengths of the S_2 ← S_0 and S_1 ← S_0 electric dipole transitions are substantially smaller for the S_0(Me → Ph) conformer than for the S_0(Me → N) conformer on an absolute scale while their absorption wavelengths are nearly identical. To give an estimate of their relative intensities, we have normalized the calculated spectra, plotted in Fig. 4, with respect to the strong ^{1}LE transition of the S_0(Me → N) conformer at *ca.* 275 nm. Qualitatively, the residual intensity of the experimental spectrum in the long wavelength regime (inset of Fig. 4) appears to match better with the absorption spectrum computed for the slightly more stable S_0(Me → Ph) conformer. The shoulder in the experimental spectra at about 315 nm originates from the S_3 ← S_0 transition. Fragment-based analyses of the DFT/MRCI wavefunctions (Fig. S5 and S8†) reveal this transition to have mixed **Tp** linker-to-**T** acceptor CT and **Tp** LE character. The high oscillator strengths of the spectral lines forming the strong absorption band between approximately 290 and 260 nm originate from local ππ* transitions. The intense lines in the 285 nm region are mainly due to ^{1}LE transitions on the **T** acceptor moiety whereas the spectrum in the 275 nm region is formed by local ^{1}ππ*(**A**) donor transitions.

The shapes and positions of the experimental bands appear to be rather insensitive with respect to the solvent polarity as seen when comparing the spectral signatures of **TpAT-tFFO** in methyl cyclohexane (MCH), toluene (PhMe) and acetonitrile (MeCN) solution.[1,2] The absorption spectrum recorded in toluene breaks off at about 300 nm where the solvent starts to absorb. At longer wavelength it is very similar to the spectra in other solvent environments. Similar observations were made for the quantum chemical modeling of the absorption. Test calculations on **TpAT-tFFO** in toluene solution led to nearly identical results as *in vacuo*, so that solvent effects have been neglected in the following. Note, however, the strong solvent-dependent Stokes shifts of the experimental emission wavelengths,[2] typical for CT transitions in liquid solution where the solvent shell can reorganize and adapt to the altered polarity of the solute in the excited state. In more rigid environments, where this reorganization is hindered at the time scale of the experiment, the experimental onset energies exhibit a much smaller variation.

3.2 Excited states

3.2.1 Geometries and electronic structures. To find a correspondence between the low-lying electronically excited states of **TpAT-tFFO** at the TDDFT (PBE0) and DFT/MRCI levels of theory, TDDFT single-point calculations at the electronic ground-state geometries of both conformers were carried out. As may be expected, the energies of the CT states (S_1, S_2, T_1 and T_2) are somewhat underestimated by the TDDFT (PBE0) calculations in comparison to DFT/MRCI, while similar excitation energies are found for the T_3 LE state. More importantly, however, the electronic structures of these five states match very well at both levels of theory (compare Tables S1, S2, S9, and S11†) so that a TDDFT (PBE0) geometry optimization of the excited states is considered meaningful. If the optimally tuned range-separated LC-ωPBE functional, employed in previous theoretical work on **TpAT-tFFO**,[1] is used instead, blue shifts of the CT state energies (Tables S10 and S12†) by about 0.2 eV in comparison to the PBE0 results are observed, but the electronic structures of the five low-lying states do not significantly change.

The optimization of the first two excited singlet states (S_1 and S_2, both CT states) and the first three excited triplet states (T_1 and T_2: CT states, T_3: LE state) yielded the desired minima on the potential energy surface (PES). Note, however, that the energetic order of the states may vary from geometry to geometry. To avoid confusion, we have kept the state designations used in the FC region of the (Me → N) conformer. For example, the locally excited triplet state is the third triplet state at the ground-state geometry. Hence, the ^{3}LE state is named T_3 and it retains this name irrespective of the energetic order at other geometries. Difference densities visualizing the characters of the electronic states at their respective minimum geometries are displayed in Fig. 5.

In general, the geometry relaxation in the excited states leads to mild changes in the tilted alignment between **A** and **T** (up to 3.0°). In detail, some dihedral angles between the triazine molecular plane and the benzene moieties of **A** change. Furthermore, a distortion of the triazine moiety itself resulting from bond length alterations with respect to the electronic ground states can be made out in all excited state structures. To provide an overview over the particular displacements of the minimum geometries, we constructed overlays of the ground and excited state structures such that their **Tp** bridges exhibit minimal root mean square deviations (Fig. 6). With regard to their minimum nuclear arrangements, the electronic states can

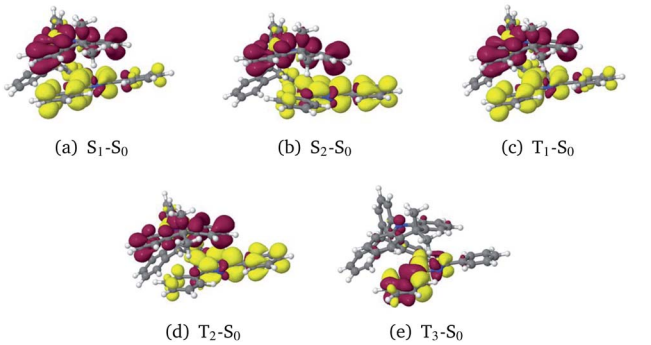

Fig. 5 Difference densities (±0.001) of the excited states at their optimized geometries. Areas losing electron density in comparison to the electronic ground state are shown in red, areas gaining electron density in yellow.

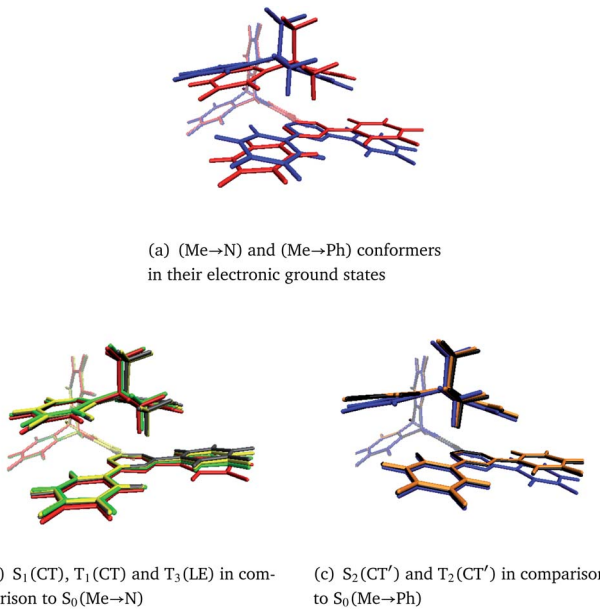

(a) (Me→N) and (Me→Ph) conformers in their electronic ground states

(b) S_1(CT), T_1(CT) and T_3(LE) in comparison to S_0(Me→N)

(c) S_2(CT′) and T_2(CT′) in comparison to S_0(Me→Ph)

Fig. 6 Overlays of TpAT-tFFO molecular frames visualizing the coordinate displacements of the respective minimum nuclear arrangements while minimizing the root mean squares deviations of the Tp bridges. The following color codes have been used: red: S_0(Me → N), blue: S_0(Me → Ph), gray: S_1(CT), yellow: T_1(CT), green: T_3(LE), orange: S_2(CT′), black: T_2(CT′). Details of the electronic structure data can be found in Tables S1–S8 and Fig. S3–S26.†

be grouped into two clusters: S_0(Me → N), S_1(CT), T_1(CT) and T_3(LE) exhibit similar relative orientations of the **A** and **T** subunits whereas S_2(CT′) and T_2(CT′) more closely resemble the S_0(Me → Ph) conformer.

Surprisingly, the energies of the S_1(CT) and S_2(CT′) states are nearly degenerate after structural relaxation to their respective minima on the PES (Table 1). In contrast, they are separated vertically by more than 0.5 eV (Fig. S27†). In terms of a Marcus-type model, a substantial reorganization energy has to be overcome for a transition between their potential energy wells. A similar picture is obtained for the corresponding excited T_1(CT) and T_2(CT′) states. On an absolute scale, the calculated adiabatic ^{1}CT and ^{3}CT energies are in good agreement with experimental on-set energies of the singlet and triplet transitions in various host matrices (Table 1). Note, however, that the calculated adiabatic ΔE_{ST} values of 0.09 eV (S_1–T_1) and 0.15 eV (S_2–T_2) are significantly larger than the singlet–triplet energy gaps derived experimentally (0.016 ± 0.002 eV) on the basis of temperature-dependent measurements in the solid state.

The potential energy scheme in Fig. S27† implies the existence of conical intersections between the CT and CT′ states which have been located at energies approximately 0.15 eV above the respective minima. Optimization of the T_3(LE) energy brings this state adiabatically into near degeneracy with the excited singlet states (0.01 eV above). Due to the closer geometric resemblance of the S_1 and T_3 structures, their reorganization energy is much smaller than for the S_2 and T_3 pair of states. While being in qualitative agreement with the scheme proposed by Kaji and co-workers on the basis of their experimental and theoretical data, the results of our computational study paint a more intricate picture of the excited-state processes in **TpAT-tFFO**.

3.2.2 Linearly interpolated paths. To obtain a better overall view of possible excited-state transition pathways, linearly interpolated potential energy profiles (LIPs) between target singlet and triplet state minima were constructed. Fig. 7a shows a relaxation pathway connecting the ground state of the (Me → N) conformer with the minimum of the S_1(CT) state. Several crossings in the vicinity of the FC region can be made out. In contrast, the energy profiles for transitions between excited singlet and triplet states with same character are very flat (Fig. S28a†). The conical intersection, found while optimizing the excited triplet states, is probably not as important for the relaxation pathway as Fig. 7c may suggest. When trying to connect the CT and CT′ states directly, we detected a pathway with much smaller activation barrier (Fig. S27b†). Thus, in liquid solution both excited ^{1}CT states can be interconverted by a simultaneous torsional motion of the **A** and **T** units about their links to the **Tp** bridge at moderate cost, similar to a deflection along mode 1 in the electronic ground state (Fig. S1†). The CI connects the two lowest excited triplet states and the two lowest excited singlet states. In the geometrical vicinity of the crossing point, S_1/T_2 and S_2/T_1 intersections with sizeable SOCMEs are found that might contribute to singlet–triplet mixing by ISC or rISC. Note, however, that – in addition to the singlet–triplet energy gap and the mutual electronic coupling of the initial and final states – the overlap of their vibrational wavefunctions is an important factor contributing to the nonradiative transition rates.[9] The S_1(CT) and T_3(LE) potentials are found to cross as well whereas T_1(CT) and T_3(LE) undergo an avoided crossing along the LIP connecting their

Table 1 Adiabatic DFT/MRCI excitation energies Δ*E* of low-lying singlet and triplet states of TpAT-tFFO in comparison with experimental on-sets in various hosts. Zero-point vibrational energy (ZPVE) corrections were computed at the (TD)DFT level of theory. All energies in eV

State		ΔE_0^0	ZPVE	Experimental on-sets[2]
S_1	CT	2.97	−0.11	2.853 (UGH-3), 2.818 (mCBP), 2.893 (CzSi), 2.943 (zeonex)
S_2	CT′	2.98	−0.12	
T_1	CT	2.88	−0.11	2.839 (UGH-3), 2.800 (mCBP), 2.877 (CzSi), 2.930 (zeonex)
T_2	CT′	2.83	−0.12	
T_3	LE	2.99	+0.04	

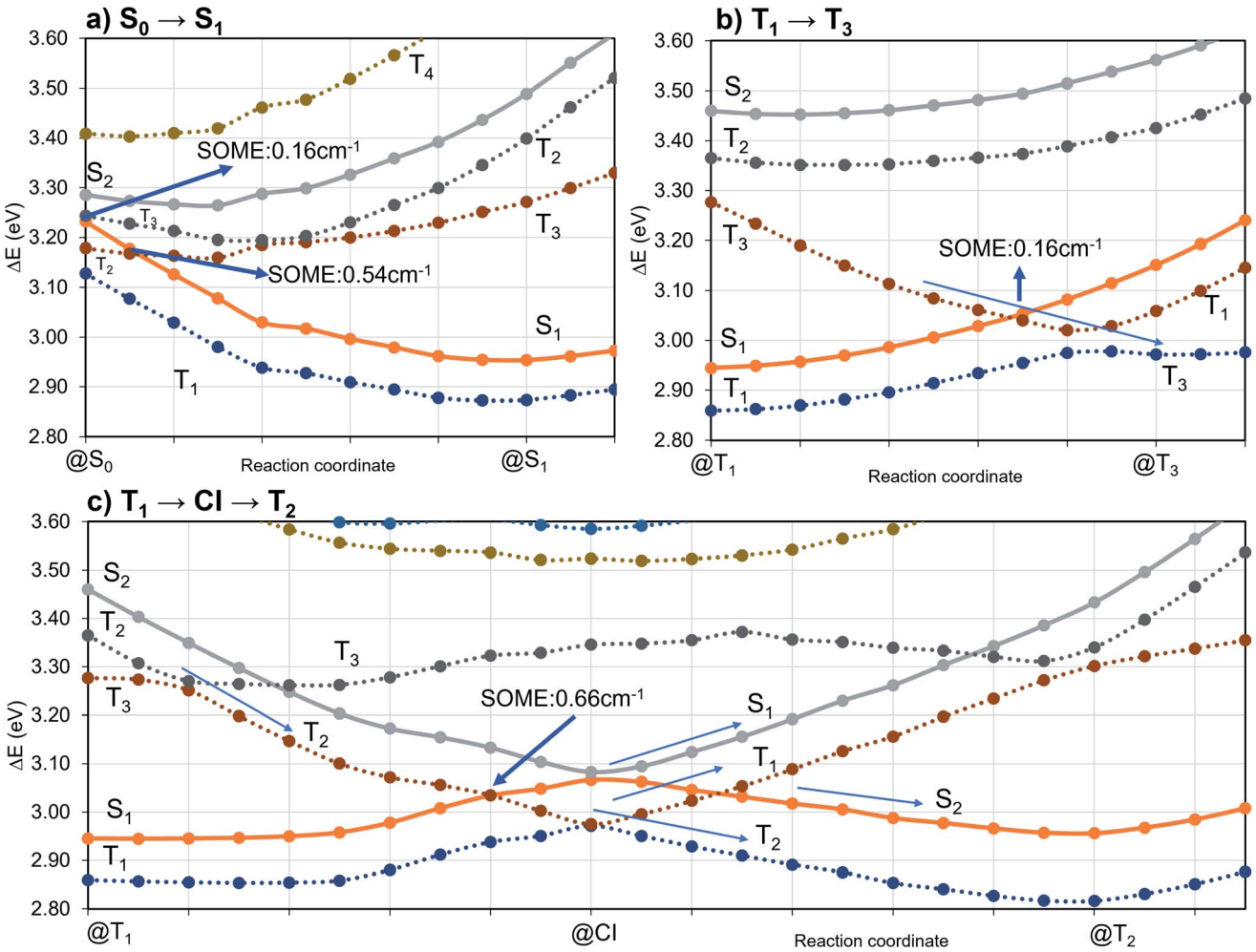

Fig. 7 DFT/MRCI energy profiles along linear interpolated pathways (LIPs) between target electronic state minima. Dashed lines correspond to triplet state PESs while solid lines correspond to singlet states.

minima (Fig. 7b). Although the SOCME between S_1 and T_3 is much smaller than for the S_1/T_2 pair of states, we will see that the T_3(LE) state plays a decisive role in the ISC and rISC kinetics of the CT states.

To investigate the importance of the tilted face-to-face alignment of the donor and acceptor units for the photophysics of **TpAT-tFFO**, the molecular frame was deflected along selected vibrational modes of the Me → N conformer, namely vibrational mode 1 (Fig. S1†), which transforms the two ground state conformers into one another, and the vibrational modes 9 and 12 (Fig. 8), which are low-frequency modes that move the donor–acceptor π-systems closer to or further away from one another. Even small distortions along these modes are sufficient to reach a crossing between S_1(CT) and T_3(LE) (Fig. S2, S29 and S30†) while the ground-state energy increases only slightly. Additionally, these vibrational motions have large impact on the oscillator strengths of the $S_1 \leftarrow S_0$ and $S_2 \leftarrow S_0$ processes. We therefore expect dynamic processes beyond the FC approximation to play an important role.

3.2.3 Emission properties. As the S_1(CT) and the S_2(CT′) states represent nearly isoenergetic minima on the PES of the first excited singlet state, both may contribute to the fluorescence. The calculations find a broad ^{1}CT emission band with maximum at 503 nm for the isolated (Me → N) conformer at 300 K in HT approximation which is blue shifted to 483 nm when cooling the molecule to 20 K. The corresponding emission maxima for the ^{1}CT emission of the (Me → Ph) conformer lie at nearly identical positions, namely at 499 nm for a sample at 300 K and 478 nm at 20 K. With a value of $k_F^{HT} \approx 1.1 \times 10^6\ s^{-1}$, the

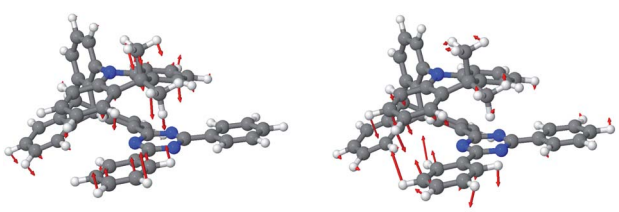

(a) mode 9, $\nu_9 = 62\ cm^{-1}$ (b) mode 12, $\nu_{12} = 83\ cm^{-1}$

Fig. 8 Low-frequency ground-state vibrational modes of the (Me → N) conformer moving the donor–acceptor π-systems closer to one another (positive deflection) or further away (negative deflection).

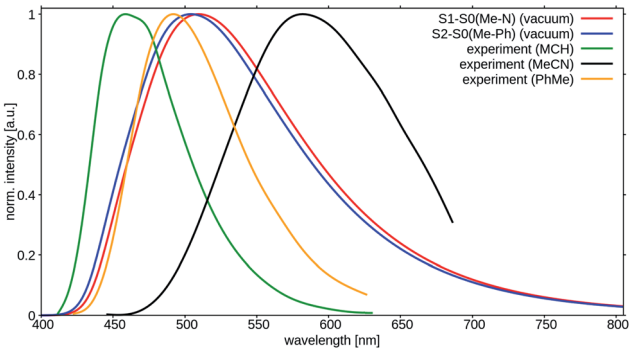

Fig. 9 Calculated room temperature fluorescence spectra of TpAT-tFFO (red: $S_1 \rightarrow S_0$ (Me → N), blue: $S_2 \rightarrow S_0$ (Me → Ph)) in comparison to experimental emission spectra in methyl cyclohexane (green), toluene (gold) and acetonitrile (black).[2]

radiative rate constant for the spontaneous fluorescence of the (Me → Ph) conformer is somewhat smaller than for the corresponding value of the (Me → N) conformer ($k_F^{HT} \approx 1.3 \times 10^6\ s^{-1}$) and might explain the occurrence of two prompt fluorescence components with essentially identical emission wavelengths in the latest experiments.[2] The HT values agree also well with the radiative rate constant of $1.1 \times 10^6\ s^{-1}$ derived experimentally by Kaji and coworkers.[1] HT coupling speeds up the fluorescence, but not to a substantial extent as may be judged from a comparison with the corresponding values in FC approximation, *i.e.*, $k_F^{FC} \approx 2.0 \times 10^5\ s^{-1}$ (Me → Ph) and corresponding value of the (Me → N) conformer ($k_F^{FC} \approx 7.0 \times 10^5\ s^{-1}$).

The peak positions of the experimental fluorescence spectra in liquid solution at RT are seen to vary substantially for different solvents (Fig. 9). The strong Stokes shift of the emission in MeCN in comparison to MCH solution is caused, for example, by the electrostatic interactions of the very polar CT state of the solute and the reorganized polar solvent environment. The fact that even the spectrum in toluene is red shifted is mostly attributed to π-stacking interactions between the solute and the solvent. Both, solvent reorganization and π-stacking effects are not included in our computational model. It is therefore not surprising that the peak positions of the computed $S_1 \rightarrow S_0$ and $S_2 \rightarrow S_0$ transitions do not agree well with the measured peak maxima in liquid solution (Fig. 9). The fact that the computed spectra show more pronounced tails in the long wavelength region than the experimental fluorescence spectrum is a consequence of the harmonic oscillator approximation that is not well obeyed by transitions involving higher vibrational levels of the electronic ground state.

Much better agreement is found when the calculated adiabatic excitation energies of the isolated molecules are compared with the experimental on-sets of the emission spectra in rigid matrices that prevent the reorganization of the solvent cage (Table 1).

In order to rationalize the long-time component of the emission observed experimentally at 20 K,[2] phosphorescence rate constants of the three low-lying triplet states were computed in FC approximation. Because vibronic interactions had only a moderate effect on the fluorescence and the computational costs for evaluating them are substantial, we refrained from computing phosphorescence in HT approximation. Component-averaged phosphorescence rate constants of $k_P^{FC} \approx 0.4 \times 10^{-1}\ s^{-1}$ (T_1), $k_P^{FC} \approx 1.0 \times 10^{-1}\ s^{-1}$ (T_2), and $k_P^{FC} \approx 8.3 \times 10^{-1}\ s^{-1}$ (T_3) were obtained corresponding to radiative lifetimes of 25 s, 10 s, and about 1 s, respectively. Looking only at the numbers, one might be tempted to attribute the emission on the 100 millisecond time scale to phosphorescence emission from the LE T_3 state that forms a shallow minimum on the first excited triplet energy surface. The LIPs in Fig. 7b suggest, however, strong nonadiabatic interactions between the T_3 and T_1 state in their crossing region energetically and geometrically close to the T_3 minimum. Moreover, motions altering the tilted face-to-face of the donor and acceptor moieties (compare Fig. S30†) lead to crossings between T_2 and T_3. It can therefore be assumed that a triplet population in the T_3 potential well rapidly relaxes *via* internal conversion to the lower-lying T_1 or T_2 states. Hence, phosphorescence is expected to originate from the ^{3}CT states and not from the ^{3}LE state. In addition to phosphorescence, $T_1(CT) \rightsquigarrow S_0$ and $T_2(CT') \rightsquigarrow S_0$ nonradiative deactivation of the triplet population will occur, explaining the difference between the observed phosphorescence decay times (100 ms regime) and the much larger theoretical lifetime values (10 s regime) which correspond to purely radiative processes.

3.2.4 Intersystem crossing. The magnitudes of the spin-component averaged SOCMEs, presented in Table 2 at various minimum geometries, suggest at first sight that the $S_1 \leftrightarrow T_2$ and $S_2 \leftrightarrow T_1$ ISC and rISC processes dominate the singlet–triplet population transfer. This is, however, not the case because their vibrational overlaps are smaller than for states belonging to the same geometrical cluster. Taking the FC factors and the energy matching conditions of the Fermi golden rule expression for the probability of a nonradiative transition into consideration yields ISC and rISC rate constants, which are two orders of magnitude too small in comparison to experiment (Table S14†). It is well known, however, that spin–vibronic interactions can substantially enhance orbitally forbidden ISC and rISC processes.[3–9] The computation of ISC and rISC rate constants of donor–acceptor compounds therefore requires to go beyond the FC approximation. Without going into details, there are two major routes to proceed, a dynamic and a static one. While the first route is optimally taken for simulating ultrafast

Table 2 Component-averaged spin–orbit matrix elements (SOCMEs, cm^{-1}) between low-lying singlet and triplet states calculated at the excited state minima of TpAT-tFFO

Interacting states	@S_1	@S_2	@T_1	@T_2	@T_3
$\langle S_1\|\hat{\mathcal{H}}_{SO}\|T_1\rangle$	0.027	—	0.039	—	—
$\langle S_1\|\hat{\mathcal{H}}_{SO}\|T_2\rangle$	0.760	—	—	0.666	—
$\langle S_1\|\hat{\mathcal{H}}_{SO}\|T_3\rangle$	0.170	—	—	—	0.142
$\langle S_2\|\hat{\mathcal{H}}_{SO}\|T_1\rangle$	—	0.581	0.750	—	—
$\langle S_2\|\hat{\mathcal{H}}_{SO}\|T_2\rangle$	—	0.082	—	0.087	—
$\langle S_2\|\hat{\mathcal{H}}_{SO}\|T_3\rangle$	—	0.348	—	—	0.299

Table 3 Rate constants for direct and vibronic ISC/rISC (s^{-1}) between low-lying singlet and triplet state minima of **TpAT-tFFO** employing their computed adiabatic energy differences

Process/ temperature	ISC/20 K	ISC/300 K	rISC/20 K	rISC/300 K
$S_1(CT) \leftrightarrow T_1(CT)$	4.3×10^5	8.8×10^5	—	$2.3 \times 10\|^4$
$S_1(CT) \leftrightarrow T_2(CT')$	2.6×10^2	3.6×10^5	—	1.7×10^3
$S_1(CT) \leftrightarrow T_3(LE)$	—	1.9×10^4	6.5×10^6	6.8×10^6
$S_2(CT') \leftrightarrow T_1(CT)$	—	1.4×10^5	—	5.2×10^3
$S_2(CT') \leftrightarrow T_2(CT')$	3.3×10^6	6.5×10^6	—	3.4×10^4
$S_2(CT') \leftrightarrow T_3(LE)$	—	1.2×10^3	2.7×10^5	8.4×10^5

nonadiabatic transitions, the static approach employed here is applicable to slower processes as it rests on a HT-type expansion of the spin–orbit interaction.[8,43,44] Derivatives of the SOCMEs with respect to normal mode displacements were determined for all states of interest, despite the high computational effort.

The inclusion of vibrational SOC commonly enhances transitions between states with the same orbital character because they can get more mixed through displacements along the vibrational modes. In this way, ISC and rISC processes can indirectly borrow intensity from El-Sayed allowed transitions and are accelerated. Although the derivative couplings of the $S_1(CT) \leftrightarrow T_1(CT)$ and $S_2(CT') \leftrightarrow T_2(CT')$ transitions are tiny (Fig. S35 and S36†), the HT terms increase the rate constants of these processes by an order of magnitude in comparison to the FC approximation. In general, the SOCME gradients for transitions between states with similar minimum nuclear arrangements are small in comparison to those for transitions between states belonging to different geometry clusters (Fig. S35–S39†). The largest SOCME gradients are found for vibrational modes located mainly on the triazine acceptor unit of **TpAT-tFFO**. Contrary to the expectations, the fastest ISC is calculated for the transition from $S_2(CT')$ to $T_2(CT')$ which is associated with the largest energy gap (Table 3). In addition, the $S_1(CT) \leftarrow T_3(LE)$ rISC rate constant reaches values of the order of 10^7 s^{-1}. The avoided crossing along the LIP connecting the minima of the $T_1(CT)$ and $T_3(LE)$ potentials (Fig. 7b) suggests that the $T_3(LE)$ state in turn interacts with the $T_1(CT)$ state *via* nonadiabatic coupling and thus can act a mediator in the $S_1(CT) \leftarrow T_3(LE) \leftarrow T_1(CT)$ rISC process. A strong coupling between the $T_2(CT')$ and $T_3(LE)$ pair of states is observed when the π-systems of **A** and **T** are tilted (mode 12, Fig. 8 and S30†). T_3 may therefore act as a mediator of the $S_2(CT') \leftarrow T_3(LE) \leftarrow T_2(CT')$ rISC process as well.

The cause of the largest uncertainties regarding the computed ISC and rISC rate constants relates to the magnitude of the singlet–triplet energy separation. The ΔE_{ST} values are somewhat overestimated by our quantum chemical calculations (Table 1) and therefore diminish the vibrational overlaps in the weak coupling case with nested PESs of the initial and final states. $S_1 \leftrightarrow T_1$ and $S_2 \leftrightarrow T_2$ belong to this coupling case. The results of various test calculations employing energy-shifted singlet and triplet potentials with gaps ranging from 0.02 to 0.17 eV are displayed in Fig. 10.

Following the energy gap law of the weak coupling case,[9,45] the rate constants of the $S_1 \rightsquigarrow T_1$ and $S_2 \rightsquigarrow T_2$ ISC transitions

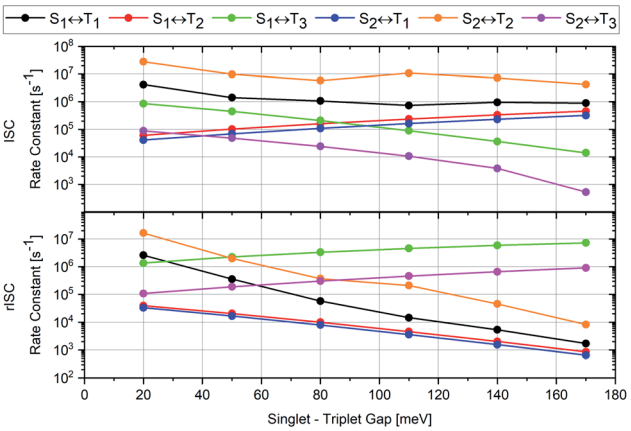

Fig. 10 Variation of the computed rate constants for ISC (upper panel) and rISC (lower panel) at 300 K with the adiabatic singlet–triplet energy separation of the initial and final states. Note the logarithmic scale of the ISC and rISC rate constants. The corresponding numerical data may be found in Tables S15 and S16.†

increase by roughly one order of magnitude when ΔE_{ST} is decreased to 0.02 eV, a value closer to the experimental estimates. As may be expected, the corresponding $S_1 \leftarrow T_1$ and $S_2 \leftarrow T_2$ rISC processes are affected even more strongly. Their rate constants are substantially enhanced when the singlet–triplet gap is reduced to 0.02 eV. Inverse trends are observed for the $S_1 \rightsquigarrow T_2$ and $S_2 \rightsquigarrow T_1$ ISC transitions which belong to the strong coupling case with substantial geometry displacements in at least some normal coordinates. Their rate constants are reduced by about one order of magnitude when the diminished. The corresponding $S_1 \leftarrow T_2$ and $S_2 \leftarrow T_1$ rISC rate constants increase, but to a much lesser extent than those of the $S_1 \leftarrow T_1$ and $S_2 \leftarrow T_2$ rISC transitions. The $S_1(CT) \rightsquigarrow T_3(LE)$ and $S_2(CT') \rightsquigarrow T_3(LE)$ ISC transitions, which are uphill processes, benefit from the reduction of the energy gap as well, but remain slower than the $S_1 \leftrightarrow T_1$ and $S_2 \leftrightarrow T_2$ ISC transitions. The corresponding downhill $S_1(CT) \leftarrow T_3(LE)$ and $S_2(CT') \leftarrow T_3(LE)$ rISC processes are less strongly affected by the potential energy shifts. Their rate constants are reduced when the singlet–triplet gap gets smaller. In both directions, the $S_1 \leftrightarrow T_3$ transitions are preferred over the $S_2 \leftrightarrow T_1$ transitions, despite their smaller electronic SOCMEs (Table 2). These examples once again underscore that is not sufficient to rely solely on the magnitude of the electronic SOCME when identifying possible ISC and rISC pathways. To get the whole picture, the inclusion of vibrational factors and vibronic interactions is mandatory for modelling ISC and rISC in donor–acceptor compounds.

4 Conclusions

All in all, the results of our quantum chemical studies support a kinetic model for the emission decay of **TpAT-tFFO** involving five electronically excited states which are coupled by spin–orbit and vibronic interactions. Three of these states, a pair of singlet and triplet CT states (S_1 and T_1) and a LE triplet state (T_3), can be associated with the (Me → N) conformer of **TpAT-tFFO**. To

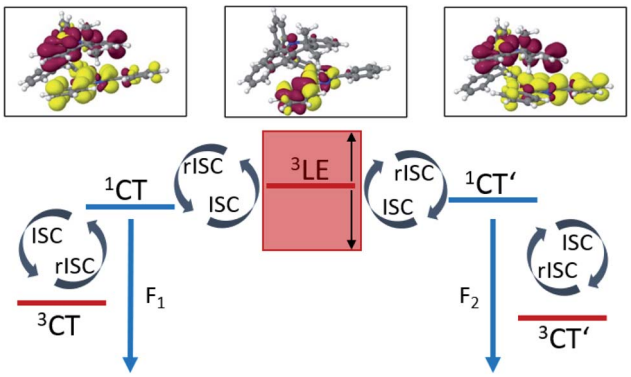

Fig. 11 Schematic excitation decay mechanism of the nearly degenerate (Me → N) and (Me → Ph) conformers of TpAT-tFFO. ISC and rISC processes are promoted by vibronic spin–orbit coupling. Low-frequency vibrations that diminish the distance between donor and acceptor π-systems tune the first excited singlet CT states of the conformers and the LE T_3 state into and out of resonance.

avoid confusion, the other two CT-type states that form the lowest excited singlet and triplet states, respectively, of the (Me → Ph) conformer, have been named S_2 and T_2 because they are the second of their kind at the ground-state geometries of both conformers. The two conformers differ in essence by the tilt angle formed by the nearly parallel **A** donor and **T** acceptor moieties with the **Tp** bridge. While the two conformers are easily interconverted in the electronic ground state – given that the environment does not sterically hinder the transformation – this is not the case in the excited state where the reorganization energy is substantial. For this reason, dual fluorescence emission may occur.

Fig. 11 summarizes the most important findings with regard to the excitation decay mechanism. The emission energies of the two excited singlet potential energy wells are nearly identical, but the radiative rate constant of the (Me → N) conformer is somewhat larger than the one of the (Me → Ph) conformer. This explains why only one emission band but two different prompt fluorescence time constants have been observed experimentally.

Like in many donor–acceptor compounds, the ISC and rISC processes between the CT states of **TpAT-tFFO** are markedly accelerated by spin-vibronic interactions with a nearby LE triplet acceptor state, T_3, located slightly above the S_1 and S_2 minima according to our calculations. While the computed ISC and rISC rate constants are sensitive with respect to the singlet–triplet energy separations, it is clear that $S_1(CT) \rightsquigarrow T_1(CT)$ and $S_2(CT') \rightsquigarrow T_2(CT')$ ISC outcompete prompt fluorescence. For singlet–triplet energy gaps larger than 0.05 eV, rISC is fastest for the $S_1(CT) \leftarrow T_3(LE)$ transition which is a slight downhill process. The avoided crossing of the $T_1(CT)$ and $T_3(LE)$ potentials suggests that the $T_3(LE)$ and $T_1(CT)$ states are strongly coupled by nonadiabatic interactions and that thus the $T_3(LE)$ state can act a mediator in the $S_1(CT) \leftarrow T_3(LE) \leftarrow T_1(CT)$ rISC process at RT. The interconversion of the CT′ states is promoted by the $T_3(LE)$ state as well. Low-frequency vibrational modes that alter the tilt angle and the interplanar distance of the donor and acceptor moieties play a decisive role in the nonadiabatic coupling of these triplet states. If the energy gaps between the lowest-lying ^{1}CT and ^{3}CT states of the (Me → N) and (Me → Ph) conformers, $S_1(CT)$–$T_1(CT)$ and $S_2(CT')$–$T_2(CT')$, are reduced to 0.02 eV, as suggested by the experimental data, the vibronically enhanced $S_1(CT) \leftrightarrow T_1(CT)$ and $S_2(CT') \leftrightarrow T_2(CT')$ mechanisms prevail at RT.

At cryogenic temperatures, the $S_1(CT) \rightsquigarrow T_1(CT)$ and $S_2(CT') \rightsquigarrow T_2(CT')$ ISC are still competitive with fluorescence whereas the corresponding rISC processes are not. $T_1(CT) \rightarrow S_0$ and $T_2(CT') \rightarrow S_0$ phosphorescence is held accountable for the long-time component of the emission observed experimentally at 20 K.

Turning our focus from the specific situation in **TpAT-tFFO** to more general aspects of the decay mechanism inherent to organic through-space charge transfer TADF emitters, our results suggest that the interplay between vibronic and spin–orbit effects is a key feature increasing the ISC and rISC probabilities in this class of chromophores. In particular, low-frequency shearing and breathing motions have the potential to alter the interplanar spacing of the donor and acceptor units and hence the energetic position of the singlet and triplet CT states in relation to low-lying triplet LE states. Intersections of the CT and LE potentials along these modes offer easy and efficient pathways for the interconversion of spin multiplicities in these light-element compounds despite the relatively small size of the spin–orbit coupling in comparison to transition metal complexes.

Data availability

Cartesian coordinates of all optimized minimum structures can be obtained upon request from the authors.

Author contributions

Jeremy M. Kaminski and Angela Rodríguez-Serrano (computational investigation, preparation of images and writing), Fabian Dinkelbach (software development and computational setup), Hector Miranda Salinas (experimental investigation and preparation of images), Andrew P. Monkman and Christel M. Marian (conceptualization, funding acquisition, project administration, supervision and writing).

Conflicts of interest

There are no conflicts to declare.

Acknowledgements

This research was funded by the Deutsche Forschungsgemeinschaft (DFG, German Research Foundation) – 396890929/GRK 2482 and MA1051/17-1. HMS acknowledges the Mexican National Council for Science and Technology, CONACYT for his studentship (2019-000021-01EXTF-00308). APM acknowledges the EPSRC for funding under grant number EP/T02240X/1.

Notes and references

1 Y. Wada, H. Nakagawa, S. Matsumoto, Y. Wakisaka and H. Kaji, *Nat. Photonics*, 2020, **14**, 643–649.

2 H. Miranda-Salinas, A. Rodriguez-Serrano, J. M. Kaminski, F. Dinkelbach, C. M. Marian and A. P. Monkman, to be published. Originally, a back-to-back publication of the experimental and theoretical studies on TpAT-tFFO in Chem. Science had been intended.

3 B. T. Lim, S. Okajima, A. Chandra and E. Lim, *Chem. Phys. Lett.*, 1981, **79**, 22–27.

4 M. Etherington, J. Gibson, H. F. Higginbotham, T. J. Penfold and A. P. Monkman, *Nat. Commun.*, 2016, **7**, 13680.

5 J. Gibson, A. P. Monkman and T. J. Penfold, *ChemPhysChem*, 2016, **17**, 2956–2961.

6 C. M. Marian, *J. Phys. Chem. C*, 2016, **120**, 3715–3721.

7 I. Lyskov and C. M. Marian, *J. Phys. Chem. C*, 2017, **121**, 21145–21153.

8 T. J. Penfold, E. Gindensperger, C. Daniel and C. M. Marian, *Chem. Rev.*, 2018, **118**, 6975–7025.

9 C. M. Marian, *Annu. Rev. Phys. Chem.*, 2021, **72**, 617–640.

10 Q. Li, J. Hu, J. Lv, X. Wang, S. Shao, L. Wang, X. Jing and F. Wang, *Angew. Chem., Int. Ed.*, 2020, **59**, 20174–20182.

11 S. Kumar, L. G. Franca, K. Stavrou, E. Crovini, D. B. Cordes, A. M. Z. Slawin, A. P. Monkman and E. Zysman-Colman, *J. Phys. Chem. Lett.*, 2021, **12**, 2820–2830.

12 Y. Song, M. Tian, R. Yu and L. He, *ACS Appl. Mater. Interfaces*, 2021, **13**, 60269–60278.

13 V. Rai-Constapel, T. Villnow, G. Ryseck, P. Gilch and C. M. Marian, *J. Phys. Chem. A*, 2014, **118**, 11708–11717.

14 T. Villnow, G. Ryseck, V. Rai-Constapel, C. M. Marian and P. Gilch, *J. Phys. Chem. A*, 2014, **118**, 11696–11707.

15 R. Mundt, T. Villnow, C. T. Ziegenbein, P. Gilch, C. Marian and V. Rai-Constapel, *Phys. Chem. Chem. Phys.*, 2016, **18**, 6637–6647.

16 M. Bracker, C. M. Marian and M. Kleinschmidt, *J. Chem. Phys.*, 2021, **155**, 014102.

17 A. Rodríguez-Serrano, F. Dinkelbach and C. M. Marian, *Phys. Chem. Chem. Phys.*, 2021, **23**, 3668–3678.

18 *TURBOMOLE V7.0 2015*, A development of University of Karlsruhe and Forschungszentrum Karlsruhe GmbH, TURBOMOLE GmbH, 1989–2007, since 2007; available from, **https://www.turbomole.com**.

19 J. P. Perdew, K. Burke and M. Ernzerhof, *Phys. Rev. Lett.*, 1996, **77**, 3865–3868.

20 C. Adamo and V. Barone, *J. Chem. Phys.*, 1999, **110**, 6158–6170.

21 S. Grimme, J. Antony, S. Ehrlich and H. Krieg, *J. Chem. Phys.*, 2010, **132**, 154104.

22 S. Grimme, S. Ehrlich and L. Goerigk, *J. Comput. Chem.*, 2011, **32**, 1456–1465.

23 E. Runge and E. K. U. Gross, *Phys. Rev. Lett.*, 1984, **52**, 997–1000.

24 M. A. L. Marques and E. K. U. Gross, *A Primer in Density Functional Theory*, Springer, Berlin, Heidelberg, 2003, pp. 144–184.

25 A. Dreuw and M. Head-Gordon, *J. Am. Chem. Soc.*, 2004, **126**, 4007–4016.

26 F. Furche and R. Ahlrichs, *J. Chem. Phys.*, 2002, **117**, 7433–7447.

27 S. Hirata and M. Head-Gordon, *Chem. Phys. Lett.*, 1999, **314**, 291–299.

28 M. J. Frisch, G. W. Trucks, H. B. Schlegel, G. E. Scuseria, M. A. Robb, J. R. Cheeseman, G. Scalmani, V. Barone, G. A. Petersson, H. Nakatsuji, X. Li, M. Caricato, A. V. Marenich, J. Bloino, B. G. Janesko, R. Gomperts, B. Mennucci, H. P. Hratchian, J. V. Ortiz, A. F. Izmaylov, J. L. Sonnenberg, D. Williams-Young, F. Ding, F. Lipparini, F. Egidi, J. Goings, B. Peng, A. Petrone, T. Henderson, D. Ranasinghe, V. G. Zakrzewski, J. Gao, N. Rega, G. Zheng, W. Liang, M. Hada, M. Ehara, K. Toyota, R. Fukuda, J. Hasegawa, M. Ishida, T. Nakajima, Y. Honda, O. Kitao, H. Nakai, T. Vreven, K. Throssell, J. A. Montgomery Jr, J. E. Peralta, F. Ogliaro, M. J. Bearpark, J. J. Heyd, E. N. Brothers, K. N. Kudin, V. N. Staroverov, T. A. Keith, R. Kobayashi, J. Normand, K. Raghavachari, A. P. Rendell, J. C. Burant, S. S. Iyengar, J. Tomasi, M. Cossi, J. M. Millam, M. Klene, C. Adamo, R. Cammi, J. W. Ochterski, R. L. Martin, K. Morokuma, O. Farkas, J. B. Foresman and D. J. Fox, *Gaussian 16, Revision A.03*, Gaussian, Inc, Wallingford CT, 2016.

29 S. Grimme and M. Waletzke, *J. Chem. Phys.*, 1999, **111**, 5645–5655.

30 C. M. Marian, A. Heil and M. Kleinschmidt, *Wiley Interdiscip. Rev.: Comput. Mol. Sci.*, 2019, **9**, e1394.

31 M. Kleinschmidt, C. M. Marian, M. Waletzke and S. Grimme, *J. Chem. Phys.*, 2009, **130**, 044708.

32 A. D. Becke, *J. Chem. Phys.*, 1993, **98**, 1372–1377.

33 C. Lee, W. Yang and R. G. Parr, *Phys. Rev. B: Condens. Matter Mater. Phys.*, 1988, **37**, 785–789.

34 I. Lyskov, M. Kleinschmidt and C. M. Marian, *J. Chem. Phys.*, 2016, **144**, 034104.

35 F. Plasser, *J. Chem. Phys.*, 2020, **152**, 084108.

36 M. Kleinschmidt, J. Tatchen and C. M. Marian, *J. Comput. Chem.*, 2002, **23**, 824–833.

37 M. Kleinschmidt and C. M. Marian, *Chem. Phys.*, 2005, **311**, 71–79.

38 M. Kleinschmidt, J. Tatchen and C. M. Marian, *J. Chem. Phys.*, 2006, **124**, 124101.

39 B. A. Heß, C. M. Marian, U. Wahlgren and O. Gropen, *Chem. Phys. Lett.*, 1996, **251**, 365–371.

40 B. Schimmelpfennig, *Atomic mean-field integral program AMFI*, University of Stockholm, 1996.

41 M. Etinski, J. Tatchen and C. M. Marian, *Phys. Chem. Chem. Phys.*, 2014, **16**, 4740.

42 M. Etinski, J. Tatchen and C. M. Marian, *J. Chem. Phys.*, 2011, **134**, 154105.

43 J. Tatchen, N. Gilka and C. M. Marian, *Phys. Chem. Chem. Phys.*, 2007, **9**, 5209.

44 M. Etinski, V. Rai-Constapel and C. M. Marian, *J. Chem. Phys.*, 2014, **140**, 114104.

45 R. Englman and J. Jortner, *Mol. Phys.*, 1970, **18**, 145–164.